SIAM J. IMAGING SCIENCES
Vol. 3, No. 4, pp. 954–980

Bochner Subordination, Logarithmic Diffusion Equations, and Blind Deconvolution of Hubble Space Telescope Imagery and Other Scientific Data*

Alfred S. Carasso†

Abstract. Generalized Linnik processes and associated logarithmic diffusion equations can be constructed by appropriate Bochner randomization of the time variable in Brownian motion and the related heat conduction equation. Remarkably, over a large but finite frequency range, generalized Linnik characteristic functions can exhibit almost Gaussian behavior near the origin, while behaving like *low exponent* isotropic Lévy stable laws away from the origin. Such behavior matches Fourier domain behavior in a large class of real blurred images of considerable scientific interest, including Hubble space telescope imagery and scanning electron micrographs. This paper develops a powerful blind deconvolution procedure based on postulating system optical transfer functions (otfs) in the form of generalized Linnik characteristic functions. The system otf and "true" sharp image are then reconstructed by solving a related logarithmic diffusion equation backward in time, using the blurred image as data at time $t = 1$. The present methodology significantly improves upon previous work based on system otfs in the form of Lévy stable characteristic functions. Such improvement is validated by the substantially smaller image Lipschitz exponents that ensue, confirming increased fine structure recovery. These results resolve the unexplained appearance of exceptionally low Lévy stable exponents in previous work on the same class of images. The paper is illustrated with striking enhancements of gray-scale and colored images.

Key words. image deblurring, blind deconvolution, Bochner subordination, generalized Linnik laws, low exponent Lévy stable laws, fractional and logarithmic diffusion equations, Lipschitz exponents, Hubble space telescope, scanning electron microscope, Whirlpool galaxy, Starburst galaxy

AMS subject classifications. 35R25, 35B60, 60E07, 68U10

DOI. 10.1137/090780225

1. Introduction.

This paper deals with blind deconvolution of a class of *real blurred* images of considerable scientific interest, as opposed to synthetically degraded phantoms. A preselected class of trial optical transfer functions (otfs), not previously known in image analysis, is shown to produce striking enhancements of Hubble space telescope images and other astronomical data, as well as useful sharpening of scanning electron micrographs of interest in Nanotechnology. Such improvements may not be apparent in the reduced size images in the printed copy of this paper. However, significant enhancement becomes evident when the *on-line* version of this paper is viewed at full size on a modern high resolution device, such as a wide screen, active matrix, liquid crystal display (LCD) monitor. As noted below, this

*Received by the editors December 16, 2009; accepted for publication (in revised form) September 15, 2010; published electronically November 30, 2010.

http://www.siam.org/journals/siims/3-4/78022.html

†Applied and Computational Mathematics Division, National Institute of Standards and Technology, Gaithersburg, MD 20899 (alfred.carasso@nist.gov).

degree of fine structure reconstruction is difficult to achieve with existing techniques.

The term *characteristic function* used in this paper refers exclusively to the Fourier transform of a probability density function [18], [27]. Such an object has distinct mathematical properties not shared by Fourier transforms of general L^1 functions [4]. Optical transfer functions are examples of characteristic functions [9]. The types of otfs considered here can be viewed as Fourier transforms of Green's functions for generalized diffusion equations, just as a Gaussian distribution is the Green's function for a heat conduction equation. These otfs belong to the class of *infinitely divisible* characteristic functions [18], [27], [32]. Deconvolution with such otfs can be accomplished in *slow motion* by solving the associated generalized diffusion equation backward in time. This is useful in the blind problem. However, this approach is not applicable to classical defocus or motion blurs, because the associated otfs are not infinitely divisible.

Blind deconvolution seeks to deblur an image without knowing the cause of the blur. An ideal mathematical approach to this problem would be based on formulating an appropriate variational principle, whereby both the unknown sharp image and the unknown blur can simultaneously be obtained as the unique minimum of a suitable energy functional. This functional should incorporate effective regularizing constraints that can stabilize ill-posedness without unduly restricting the class of admissible solutions. However, for the present class of problems, such variational approaches thus far proposed have had very limited success. This is discussed later. The more productive methodology developed here is based on identifying a plausible blurring otf from within a restricted class of candidate blurs. Slow motion deconvolution plays an essential role in this identification. The choice of trial otfs is governed by the Fourier domain behavior in the blurred imagery under consideration. In general, the results of any blind deconvolution procedure on *real* data must be viewed as producing a *hypothetical* true image and blur. There can be no assurance that the *actual* true image and blur satisfy the a priori constraints incorporated in an energy functional, or the assumptions underlying the present methodology. As in other real inverse problems, the value of such hypothetical results must subsequently be assessed by experienced analysts, using independent considerations.

Previous work on the above class of problems [10], [11] was based on candidate otfs in the form of isotropic Lévy stable characteristic functions [18], [27], [31] and the use of time-reversed diffusion equations involving fractional powers of the negative Laplacian. An important observation in [7], [10], [11] is that the successful deblurring otfs are characterized by low Lévy exponents, with typical values less than 0.5, while Gaussian otfs have exponent 2. Such low values are quite exceptional in applications where Lévy stable laws appear. The physical origin, if any, of such exponent values is not known. The present method is based on otfs in the form of generalized Linnik characteristic functions [16], [26], [32] and the use of time-reversed diffusion equations involving the *logarithm* of the negative Laplacian plus the identity. Linnik otfs have distinctly different behavior near the origin than do Lévy stable otfs. We show that this results in higher quality reconstructions than previously obtained. This improvement in fine structure recovery can be quantified by measuring the resulting decrease in image Lipschitz exponents [8], [13]. Moreover, the high frequency behavior in the successful Linnik deblurring otfs resolves the previously unexplained appearance of low Lévy exponents in [10] and [11].

Brownian motion, represented by Gaussian probability distributions, is pervasive in many

branches of science, and Gaussian otfs are ubiquitous in image reconstruction. However, the frequent occurrence of Lévy stable motion in many areas of application, including image science, is equally noteworthy. Such motion may be interpreted as Brownian motion taking place in a specific randomized time [18]. The resulting heavy-tailed probability distribution is often found to be a better physical model than the Gaussian distribution. Randomized Brownian motion is an example of Bochner *subordination* of stochastic processes [5], [6], [18], [32], whereby a given Markov process $\mathbf{X}(t)$, $t > 0$, is observed in new stochastic "operational time" $\mathbf{S}(t)$, rather than in standard clock time t, resulting in the process $\mathbf{X}(\mathbf{S}(t))$. This concept has been found fruitful in several branches of science, engineering, and finance [1], [15], [19], [20], [35]. In that context, generalized Linnik characteristic functions describe the family of processes obtained when isotropic Lévy stable motions are observed in the randomized operational time $\mathbf{\Gamma}(t)$, where for each $t > 0$, $\mathbf{\Gamma}(t)$ obeys a Gamma distribution on $u \geq 0$. The important special case of Brownian motion observed in stochastic time $\mathbf{\Gamma}(t)$ is called the *Variance Gamma Process* [28], [29]. This has been used successfully in option pricing.

Image acquisition involves the interaction of several interfacing optical and electronic devices, each producing a small distortion of the input signal. Additional aberrations may result from the scattering properties of the medium through which radiation propagates. A significant empirical discovery [21], [22], [23] is that a large variety of electro-optical imaging devices have otfs given by Lévy stable characteristic functions. Very recently [3], an optical material was created with a specific kind of inhomogeneity, in which the scattering of light waves results in Lévy flights rather than Brownian motion. A prescribed Lévy exponent for this scattering process can be engineered by proper synthesis of the inhomogeneity. As already noted, Lévy stable motions are related to Brownian motion through Bochner subordination. A second subordination, involving the $\mathbf{\Gamma}(t)$ process, would result in generalized Linnik otfs. Conceivably, Linnik otfs may play an unsuspected role in many imaging situations.

Bochner subordination also plays an important role in operator semigroup theory and evolutionary partial differential equations. By combining subordination with the Hille–Yosida theorem, a functional calculus for semigroup generators is developed in [30], whereby entirely new semigroups can be created by randomizing the time variable. See also [12]. We shall use this functional calculus to construct the relevant diffusion equations in our slow motion deconvolution procedure.

The blind deconvolution procedure presented here is fundamentally different from such variational blind formulations as [14] and [24]. These methods aim to solve the blind deconvolution problem in full generality, by minimizing an appropriate cost functional. Such techniques do not appear useful for the present class of problems. The method in [14] is primarily intended for "blocky" images and for point spread functions with edges. Astronomical images are typically diffuse and partly amorphous and are very far from being of bounded variation. Use of [14] tends to eliminate individual star clusters and other localized bright areas, which are interpreted as unwanted noise. The method in [24] requires a prior guess for the system otf. However, even with a good guess, this method often returns a questionable sharp image associated with a new, but physically impossible, otf [9]. Other more promising approaches, such as [2], exploit prior knowledge of the edge map in the unknown image. Most galaxy images lack well-defined sharp edges.

The use of generalized Linnik densities as trial blurring kernels in this paper is primarily

motivated by their mathematical properties. The semigroup property of *infinite divisibility* [18], [27], [32], the Fourier domain Gaussian-like behavior near the origin, together with the monotone convex high frequency behavior which imitates the blurred image data, all play essential roles. We do not claim an actual physical basis for Linnik otfs, and the significance of this paper ultimately rests on the quality of the reconstructions. However, our results strongly suggest a possible physical basis for such Linnik otfs, mediated by subordination as in previously mentioned applications. These otfs appear to mimic the behavior of the true otfs sufficiently well to produce credible results.

If and when comprehensive blind deconvolution methods become available, the methodology presented here is likely to remain useful. It can provide independent reconstructions for comparison, and it can provide valuable initial guesses that might be refined by more elaborate procedures.

2. Convolution blurring of images and conservation of L^1 norms. All images in this paper are 8-bit images, with pixel values scaled from 0 to 255. Given an image $g(x,y)$, we define its Fourier transform by

$$\hat{g}(\xi,\eta) \equiv \int_{R^2} g(x,y)e^{-2\pi i(\xi x+\eta y)}dxdy, \tag{1}$$

and we denote by $\| g \|_r$ the $L^r(R^2)$ norm of $g(x,y)$. Typically, $r = 1$ or 2. We also use the "total variation" seminorm

$$\| g \|_{TV} \equiv \| \nabla g \|_1. \tag{2}$$

In general, a real blurred image $g(x,y)$ contains noise $n(x,y)$ which may be signal-dependent:

$$g(x,y) = g_e(x,y) + n(x,y), \qquad \| n \|_r \ll \| g_e \|_r, \quad r = 1,2. \tag{3}$$

Here, $g_e(x,y)$ denotes the exact blurred image that would have been recorded in the absence of any errors or noise, and $n(x,y)$, assumed small, may be a nonlinear function of $g_e(x,y)$. Neither $g_e(x,y)$ nor $n(x,y)$ are known; only their sum $g(x,y)$ is known.

We assume the blurred image $g(x,y)$ to result from convolution of the true sharp image $f(x,y)$ with a *shift-invariant* point spread function (psf) $h(x,y)$,

$$g(x,y) = \int_{R^2} h(x-u,y-v)f(u,v)dudv \equiv h \otimes f, \tag{4}$$

where $\otimes$ denotes convolution on $L^1(R^2)$. The psf $h(x,y)$ is a probability density function, since it is nonnegative and integrates to unity. Because $f(x,y),\ g(x,y) \geq 0$, it follows from (4) that $\| g \|_1 = \| f \|_1$. Thus convolution of f with h conserves L^1 norms. However, given $g(x,y) = h \otimes f$, *deconvolution* of g with some point spread function $k(x,y) \neq h(x,y)$ need not conserve L^1 norms, even in the absence of noise. This may be seen as follows using Fourier transforms. Let $f(x,y) \in L^1(R^2)$ be an image with sharp edges and fine structure, let $h(x,y)$ be the Gaussian psf with Fourier transform $\exp\{-(\xi^2+\eta^2)\}$, and let $k(x,y) = h \otimes h$. Then, if $g = h \otimes f$, then

$$\begin{aligned} &\hat{g}(\xi,\eta) = \exp\{-(\xi^2+\eta^2)\}\hat{f}(\xi,\eta), \\ &\hat{f}^{\dagger}(\xi,\eta) = \exp\{2(\xi^2+\eta^2)\}\hat{g}(\xi,\eta) = \exp\{(\xi^2+\eta^2)\}\hat{f}(\xi,\eta). \end{aligned} \tag{5}$$

Clearly, $\hat{f}^{\dagger}(\xi,\eta)$ is not the Fourier transform of an image in $L^1(R^2)$ if $\hat{f}(\xi,\eta)$ decays too slowly at ∞.

3. Imagery with monotone Fourier decay and positive monotone otfs. While the psf $h(x,y)$ in (4) is always nonnegative, the otf $\hat{h}(\xi,\eta)$ is complex-valued in general. However, there is a large class of *isotropic* otfs $\hat{h}(\xi,\eta)=\hat{h}(\rho),\ \rho=\sqrt{\xi^2+\eta^2}$, which are also *positive and monotone decreasing*. This follows from Schoenberg's theorem on completely monotone functions [17], [33]. Gaussians are the best-known prototype of such otfs. This paper seeks to identify objects $\hat{h}_{app}(\rho)$ in that class that can successfully capture the essential aspects of the possibly more complex true otfs $\hat{h}_{true}(\xi,\eta)$ and result in useful reconstructions.

The example in Figure 1 is representative of a large class of images of galaxies and other astronomical objects and serves to motivate the ideas behind the method. An original 512×512 pixel Pleiades (M45) image $g(x,y)$ is shown on the left-hand side at the top of Figure 1. The deblurred image on the right-hand side is a good representation of a sharp Pleiades image $f(x,y)$, and we shall consider $f(x,y)$ to be the "true" Pleiades image for the purpose of this discussion. It is instructive to compare the corresponding Fourier images $\hat{g}(\xi,\eta),\ \hat{f}(\xi,\eta)$. Of particular interest are the plots of $\log|\hat{g}(\xi,0)|$ and $\log|\hat{f}(\xi,0)|$ vs. $|\xi|$, shown as the blue curves in the middle part of Figure 1. While these blue traces are locally highly oscillatory, they are *globally monotone decreasing and convex*, as even functions of ξ. The red curves $p(\xi)$ and $q(\xi)$ capture the gross behavior in the blue traces away from the origin. The curve p decays faster than the curve q. Both p and q were chosen so as to have a maximum value of 0, attained at $\xi=0$. In addition, as shown in the bottom drawing in Figure 1, the curves $\log|\hat{g}(\xi,0)|$ and $\log|\hat{f}(\xi,0)|$ are such that away from the origin, the ratio of these two quantities remains fairly constant, fluctuating around some mean value larger than 1. Accordingly,

$$\begin{aligned}&\log|\hat{g}(\xi,0)|/\log|\hat{f}(\xi,0)|\approx \mathit{Constant}>1, \qquad |\xi|\gg 1,\\ &p(\xi)/q(\xi)\approx \mathit{Constant}>1, \qquad |\xi|\gg 1.\end{aligned} \tag{6}$$

A comparison of the left- and right-hand sides in Figure 1 leads to the following. Assume that the original image $g(x,y)$ on the left is the convolution of the true image $f(x,y)$ on the right, with a psf $h_{true}(x,y)$. We may identify possible otfs $\hat{h}_{app}(\rho)$ using

$$\begin{aligned}&g_e(x,y)+n(x,y)\equiv g(x,y)=h_{true}(x,y)\otimes f(x,y),\\ &\log|\hat{g}(\xi,\eta)|=\log|\hat{h}_{true}(\xi,\eta)|+\log|\hat{f}(\xi,\eta)|\approx\log\hat{h}_{app}(\rho)+\log|\hat{f}(\xi,\eta)|,\\ &\log|\hat{g}(\xi,0)|\approx\log\hat{h}_{app}(\rho)+\log|\hat{f}(\xi,0)|,\\ &\log|\hat{g}(\xi,0)|\sim p(\xi), \qquad \log|\hat{f}(\xi,0)|\sim q(\xi), \qquad |\xi|\gg 1,\\ &\log\hat{h}_{app}(\rho)\sim p(\rho)-q(\rho), \qquad \rho\gg 1.\end{aligned} \tag{7}$$

Thus, under the preceding assumptions, behavior in $\hat{h}_{app}(\rho)$ away from the origin can be inferred from that in $p-q$. In practice, we are given an original image $g(x,y)$ with Fourier

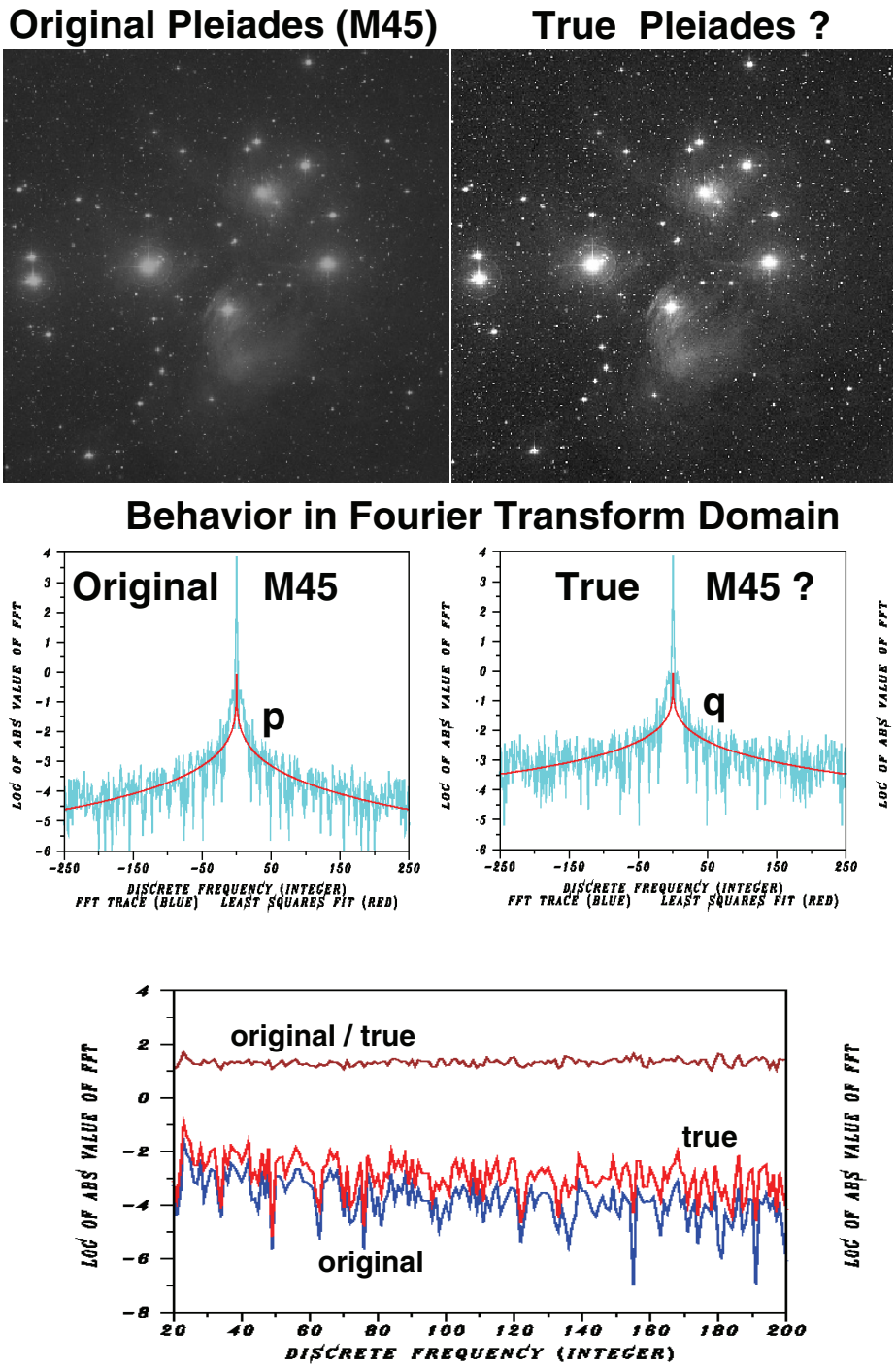

Figure 1. *The above Pleiades Fourier transform behavior is representative of a large class of images. Away from the origin, blurred image data* $\log|\hat{g}(\xi,0)|$ *on the left and "true" image data* $\log|\hat{f}(\xi,0)|$ *on the right exhibit similar highly oscillatory globally convex monotone behavior, but the left-hand data decays faster. Moreover, the ratio* $\log|\hat{g}(\xi,0)|/\log|\hat{f}(\xi,0)|$ *remains fairly constant, fluctuating around some mean value larger than unity.*

domain behavior similar to that on the left in Figure 1, but we do not have $f(x,y)$. We may find $p(\xi)$ but not $q(\xi)$. However, for a large class of blurred images $g(x,y)$, the a priori assumption that the corresponding true image $f(x,y)$ has Fourier behavior similar to that on the right of Figure 1, and obeys (6), is found to lead to useful reconstructions. Accordingly, using (6) and (7) together with $g(x,y)$, we postulate that with some *unknown constant* c, $0 < c < 1$,

$$
\begin{aligned}
&q(\rho) \sim cp(\rho), \qquad \rho \gg 1, \\
&\log \hat{h}_{app}(\rho) \sim (1-c)p(\rho), \qquad \rho \gg 1.
\end{aligned}
\tag{8}
$$

3.1. Unknown parameter in candidate otfs. Not all images $g(x,y)$ display the globally monotone decreasing Fourier domain behavior shown in Figure 1, but important classes of images share this property [7]. For such images, following the development leading to (8) above, we use nonlinear least squares to fit the data $\log|\hat{g}(\xi,0)|$ with a suitable monotone decreasing function $p(\xi)$ with $p(0) = 0$. We next seek to locate a candidate otf $\hat{h}(\rho)$ by finding the right constant c, such that $\log \hat{h}(\rho) = (1-c)p(\rho)$. This implies a restriction on $p(\rho)$, which must be such that for any constant b with $0 < b < 1$, the function $bp(\rho)$ is the logarithm of a characteristic function. This is the case if and only if $\exp\{p(\rho)\}$ is an *infinitely divisible* characteristic function [18], [27]. As may be anticipated from (5) above, and will be fully discussed in section 5 below, the unknown positive constant c in (8) can be determined by marching an appropriate generalized diffusion equation backward in time and monitoring conservation of L^1 norms as $t \downarrow 0$.

4. Infinitely divisible otfs and subordinated diffusion equations. In the deconvolution problem $h(x,y) \otimes f(x,y) = g(x,y)$, the targeted class of images exhibits globally monotone Fourier decay. Accordingly, we direct attention to candidate otfs from the following three types of infinitely divisible, isotropic monotone characteristic functions:

$$
\begin{aligned}
&\hat{h}(\rho) = \exp(-\sigma\rho^2), \quad \sigma > 0, \quad \rho = \sqrt{\xi^2+\eta^2} \qquad \text{(Gaussian)}, \\
&\hat{h}(\rho) = \exp(-\sigma\rho^\alpha), \quad \sigma > 0, \quad 0 < \alpha \le 2 \qquad \text{(Lévy stable)}, \\
&\hat{h}(\rho) = (1+\sigma\rho^\alpha)^{-\lambda}, \quad \sigma,\ \lambda > 0, \quad 0 < \alpha \le 2 \qquad \text{(generalized Linnik)}.
\end{aligned}
\tag{9}
$$

These three otf types satisfy Schoenberg's theorem [17], [33]. In physical (x,y) space, the corresponding psfs are isotropic bell-shaped surfaces with distinct tail behavior. Typical examples of each of the three types of psfs are shown in Figure 2. The non-Gaussian psfs are heavy-tailed probability density functions. Each of these three types is associated with a diffusion equation. The Gaussian case, representing Brownian motion, corresponds to the heat equation, as is well known. The other two types involve stochastic processes and corresponding diffusion equations that result from randomizing the time variable in Brownian motion. We shall show this by introducing the notion of the *subordinated semigroup* [12], [30], [32] together with the functional calculus that constructs the associated evolution equation.

Consider a family of functions $\{p_t(u)\}$ indexed by $t \ge 0$ and defined on $u \ge 0$, and such that for each fixed $t > 0$, $p_t(u)$ is a probability density function on $u \ge 0$. Assume that

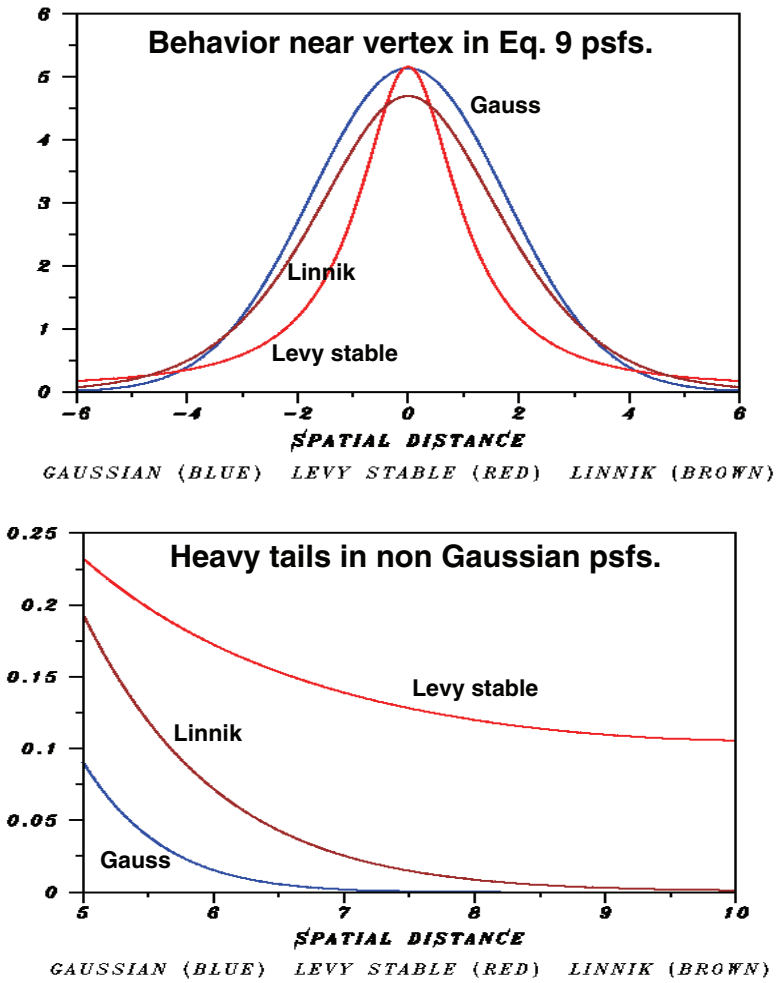

Figure 2. *Typical point spread functions corresponding to each of the three otf types in (9). Generalized Linnik (brown) and Lévy stable (red) psfs exhibit heavier tails than the Gaussian psf (blue).*

$p_t(u) * *p_s(u) = p_{t+s}(u)$, where $**$ denotes convolution on $u \geq 0$, and that $p_t(u) \to \delta(u)$ as $t \downarrow 0$. For fixed $t > 0$, the Laplace transform of $p_t(u)$ is defined by

$$\mathcal{L}(p_t) = \int_0^\infty p_t(u) e^{-uz} du, \qquad \text{Re } z > 0. \tag{10}$$

Definition 1. *A Bochner subordinator is a family $\{p_t(u)\}$ as defined above, such that $\mathcal{L}(p_t) = \exp\{-t\psi(z)\}$, where $\psi(z)$ is holomorphic for* Re $z > 0$ *and continuous for* Re $z \geq 0$, *with* Re $\psi(z) \geq 0$. *Moreover, $\psi(0) = 0$, and $\psi'(x)$ is completely monotone on $x > 0$. The function $\psi(z)$ is called the Bernstein function.*

The following two subordinator examples, involving the Gamma and Inverse Gaussian

families, respectively, yield closed form expressions:

$$
\begin{aligned}
&p_t(u) = \{\Gamma(\lambda t)\}^{-1}\sigma^{-\lambda t}u^{\lambda t-1}e^{-u/\sigma}, \quad \sigma,\ \lambda > 0, \qquad \mathcal{L}(p_t) = (1+\sigma z)^{-\lambda t},\\
&p_t(u) = \{te^{-t^2/4u}\}/\sqrt{4\pi u^3}, \qquad \mathcal{L}(p_t) = e^{-t\sqrt{z}}.
\end{aligned}
\tag{11}
$$

The Inverse Gaussian is the special case $\beta = 1/2$ of the important Lévy subordinator family of index β, where $0 < \beta \leq 1$. For $\beta \neq 1/2$, this subordinator is not known in closed form and is defined implicitly by

$$
p_t(u) = \mathcal{L}^{-1}(e^{-tz^\beta}), \qquad \text{Re } z > 0. \tag{12}
$$

In the above, whenever multivalued Bernstein functions $\psi(z)$ appear, the particular branch of $\psi(z)$ such that Re $\psi(z) > 0$ on Re $z > 0$ is always understood.

Let $U(t)$ be the operator semigroup e^{-tA} associated with the well-posed linear evolution equation $w_t = -Aw,\ t > 0,\ w(0) = f$ in a Banach space B. Bochner subordination involves *randomizing the time variable* in $U(t)$ as follows. Let $\{p_t(u)\}$ be a Bochner subordinator with Bernstein function $\psi(z)$, and define a new semigroup $T(t)$ by

$$
\begin{aligned}
T(t)f &= \int_0^\infty p_t(s)U(s)f\,ds, \qquad f \in B,\\
&= \int_0^\infty p_t(s)e^{-tA}f\,ds = e^{-t\psi(A)}f,
\end{aligned}
\tag{13}
$$

on using $\mathcal{L}(p_t) = \exp\{-t\psi(z)\}$. Thus, formally, if $U(t) = e^{-tA}$, the subordinated semigroup $T(t)$ is the semigroup $e^{-t\psi(A)}$ associated with the well-posed linear evolution equation $w_t = -\psi(A)w,\ t > 0,\ w(0) = f$. See [12], [30], [32].

4.1. Subordinated Green's functions. Let A be a linear partial differential operator in the space variables in R^2, with *constant coefficients*. Let $\hat{h}(\xi,\eta,t)$ denote the Fourier transform of the Green's function for the linear evolution equation $w_t = -Aw$. The Green's function $\hat{h}_\psi(\xi,\eta,t)$ for $w_t = -\psi(A)w$ can be obtained from $\hat{h}(\xi,\eta,t)$, using the composition law for subordinated characteristic functions [32, Chapter 6],

$$
\hat{h}_\psi(\xi,\eta,t) = \exp\left[-t\psi(-\log\{\hat{h}(\xi,\eta,1)\})\right]. \tag{14}
$$

We may now apply the foregoing analysis together with (14) to identify the diffusion equations $w_t = -\psi(A)w$ associated with (9). We begin with the well-posed forward heat equation and its Gaussian Green's function

$$
\begin{aligned}
&w_t = a\Delta w, \quad t > 0, \quad a > 0,\\
&\hat{h}(\xi,\eta,t) = \exp(-t\sigma\rho^2), \quad \sigma = 4a\pi^2, \qquad \rho = \sqrt{\xi^2+\eta^2}.
\end{aligned}
\tag{15}
$$

Lévy subordination with $\psi(z) = z^\beta$ in (15) leads to a well-posed forward fractional diffusion equation, with a Lévy stable Green's function

$$
\begin{aligned}
&w_t = -\left[b(-\Delta)^\beta\right]w, \quad t > 0, \quad b > 0, \qquad 0 < \beta \leq 1,\\
&\hat{h}(\xi,\eta,t) = \exp(-t\delta\rho^{2\beta}), \quad \delta = b(4\pi^2)^\beta, \qquad \rho = \sqrt{\xi^2+\eta^2}.
\end{aligned}
\tag{16}
$$

Next, Gamma subordination with $\psi(z) = \lambda \log\{1+\sigma z\}$ in (16) results in a well-posed forward logarithmic diffusion equation, with a generalized Linnik Green's function

$$
\begin{aligned}
&w_t = -\left[\lambda \log\{1 + c(-\Delta)^{\beta}\}\right] w, \quad t > 0, \quad c > 0, \qquad 0 < \beta \le 1, \\
&\hat{h}(\xi, \eta, t) = (1 + \gamma \rho^{2\beta})^{-\lambda t}, \quad \gamma = c(4\pi^2)^{\beta}, \qquad \rho = \sqrt{\xi^2 + \eta^2}.
\end{aligned} \tag{17}
$$

The generalized Linnik process may also be viewed as resulting from a single subordination of Brownian motion with the Bernstein function $\psi(z) = \lambda \log(1 + \sigma z^{\beta})$.

4.2. Backward diffusion equations. Given the blurred image $g(x, y)$, consider the deconvolution problem $h(x, y) \otimes f(x, y) = g(x, y)$, where the otf $\hat{h}(\xi, \eta)$ is *known* and corresponds to one of the three types in (9). We may view $\hat{h}(\xi, \eta)$ as the Green's function $\hat{h}(\xi, \eta, t)$ at time $t = 1$, in the corresponding forward evolution equation $w_t = -Lw$, in one of (15), (16), or (17). Deconvolution is mathematically equivalent to solving $w_t = -Lw$ backward in time, given the noisy blurred image $g(x, y)$ as data at time $t = 1$. For $0 < t < 1$, $w(x, y, t)$ is a partially deblurred image. The fully deblurred image $f(x, y)$ is the solution at time $t = 0$.

Such backward continuation in diffusion equations is notoriously ill-posed. The SECB method (see [25] for an up-to-date discussion) is a well-regularized continuation procedure that takes into account the presence of noise in $g(x, y)$ at $t = 1$. With $n(x, y)$ as in (3), let constants $\epsilon,\ M$ be given such that

$$
\| w(0) \|_2 \equiv \| f \|_2 \le M, \qquad \| w(1) - g \|_2 \equiv \| n \|_2 \le \epsilon, \qquad \epsilon \ll M. \tag{18}
$$

For any constant $K > 0$ such that $K \ll M/\epsilon$ define s^* by

$$
s^* = \log\{M/(M - K\epsilon)\} / \log(M/\epsilon). \tag{19}
$$

The *slow evolution* constraint applied to the backward solution of $w_t = -Lw$ requires that there exist a known constant $K,\ 0 < K \ll M/\epsilon$, and a known fixed $s \gg s^*$, such that

$$
\| w(s) - w(0) \|_2 \le K\epsilon. \tag{20}
$$

Let $T(t),\ t \ge 0$, be the solution operator corresponding to $w_t = -Lw$. Given the regularization parameters K and s, the SECB solution to the backward problem is $w^{\dagger}(x, y, t) = T(t) f^{\dagger}(x, y)$, where $f^{\dagger}(x, y)$ is that initial value $w^{\dagger}(x, y, 0)$ which *minimizes*

$$
\| w(1) - g \|_2^2 + K^{-2} \| w(s) - w(0) \|_2^2 \tag{21}
$$

over all choices of initial values $w(x, y, 0)$ in L^2. We may express $f^{\dagger}(x, y)$ in (21) in terms of $T(t)$ as follows:

$$
f^{\dagger}(x, y) = \mathrm{Argmin}_{f \in L^2} \left\{ \| T(1) f - g \|_2^2 + K^{-2} \| (T(s) - I) f \|_2^2 \right\}. \tag{22}
$$

This leads to the following Euler–Lagrange equation for $f^{\dagger}(x, y)$:

$$
\left\{ T(1)^* T(1) + K^{-2} (T(s) - I)^* (T(s) - I) \right\} f^{\dagger} = T(1)^* g. \tag{23}
$$

With $\hat{h}(\xi,\eta,t)$ the Fourier transform of the Green's function for $w_t = -Lw$, we have $\widehat{T(t)f} = \hat{h}(\xi,\eta,t)\hat{f}(\xi,\eta)$. We may use (23) to find the fully deblurred SECB image $f^\dagger(x,y)$ in closed form in the Fourier transform domain. We have, with $\overline{z}$ denoting the complex conjugate of z,

$$\hat{f}^\dagger(\xi,\eta) = \frac{\overline{\hat{h}}(\xi,\eta,1)\ \hat{g}(\xi,\eta)}{|\hat{h}(\xi,\eta,1)|^2 + K^{-2}|1-\hat{h}(\xi,\eta,s)|^2}, \tag{24}$$

leading to $f^\dagger(x,y)$ upon inverse transforming. The partially deblurred SECB image $w^\dagger(x,y,t)$ is then defined by

$$\hat{w}^\dagger(\xi,\eta,t) = \frac{\hat{h}(\xi,\eta,t)\ \overline{\hat{h}}(\xi,\eta,1)\ \hat{g}(\xi,\eta)}{|\hat{h}(\xi,\eta,1)|^2 + K^{-2}|1-\hat{h}(\xi,\eta,s)|^2}, \qquad 0 \le t < 1. \tag{25}$$

In the present case of isotropic positive otfs $\hat{h}(\rho,t)$, $\rho = \sqrt{\xi^2+\eta^2}$, we may dispense with complex conjugates and absolute values in (25) and obtain the simpler form

$$\hat{w}^\dagger(\xi,\eta,t) = \frac{\hat{h}(\rho,t)\ \hat{h}(\rho,1)\ \hat{g}(\xi,\eta)}{\hat{h}^2(\rho,1) + K^{-2}(1-\hat{h}(\rho,s))^2}, \qquad 0 \le t < 1. \tag{26}$$

4.3. Marching backward in time in Fourier space. With the blurred image $g(x,y)$ as data at time $t=1$, the SECB method can be efficiently implemented as a marching procedure in Fourier space, using FFT algorithms. Fix a positive integer N, let $\tau = 1/N$, and let $R(\rho) = \{\hat{h}(\rho,1)\}^{-\tau}$. Let $t_n = 1 - n\tau$, $n = 0,1,\ldots,N$. Then, $t_0 = 1$, and $t_N = 0$. One can generate the solution in (26) by marching backward in time from $t=1$ to $t=0$, recursively, as follows:

$$\begin{aligned} &\hat{w}(\xi,\eta,t_0) = \hat{h}^2(\rho,1)\hat{g}(\xi,\eta)/\{\hat{h}^2(\rho,1) + K^{-2}(1-\hat{h}(\rho,s))^2\}, \\ &\hat{w}(\xi,\eta,t_n) = R(\rho)\hat{w}(\xi,\eta,t_{n-1}), \qquad n = 1,\ldots,N. \end{aligned} \tag{27}$$

4.4. Choosing the regularization parameters K and s in (21). This requires a good guess for the ratio M/ϵ, and $K \ll M/\epsilon$ should be chosen as large as possible. However, real blurred images contain signal-dependent noise $n(x,y)$ that may be difficult to characterize and estimate. With the blurred image $g(x,y)$ as data at time $t=1$, a good strategy is to fix $s = 0.001$, say, and then adjust K interactively. Increasing K increases fine scale resolution in the deblurred image, but too large a value of K brings out noise as $t \downarrow 0$. Several trials are typically necessary to properly tune K and s. In the deblurring experiments discussed below, s is fixed at the value $s = 0.001$, and K ranges from $K = 40$ to $K = 100$.

5. Blind deconvolution. Identifying the unknown constant in (8) by marching backward in time. Conservation of L^1 norms. The developments in the previous section presuppose knowledge of the otf $\hat{h}(\xi,\eta,t)$. In general, as emphasized in [7, Figure 1], given a blurred $g(x,y)$, there may be a large number of distinct otfs that can competently deblur that image. In fact, the blind deconvolution problem has a multiplicity of distinct useful solutions, as well as an infinite number of meaningless solutions. A related observation is that solutions to the

blind problem obtained by minimizing a variational energy functional generally depend on the particular initial guess chosen, with different initial guesses producing different outcomes. Moreover, as shown in [9], such variational solutions may be based on physically impossible otfs and be *invalid*. Here, as indicated in section 3, given an image $g(x,y)$, we seek to identify the system otf by a least squares fit to the data $\log|\hat{g}(\xi,0)|$, with a suitable monotone decreasing function $p(\xi)$ with $p(0)=0$, as in Figure 1. The function $p(\rho)$ is chosen so that $\exp\{p(\rho)\}$ is one of the three characteristic function types in (9). From (8), the system otf we seek is given by $\exp\{(1-c)p(\rho)\}$ with an *unknown constant* c, $0<c<1$. However, we may locate useful values for c as follows. Define

$$\hat{h}(\xi,\eta,t)=\exp\{tp(\rho)\},\quad 0\le t\le 1,\qquad \rho=\sqrt{\xi^2+\eta^2}, \tag{28}$$

so that $\hat{h}(\xi,\eta,t)$ is the Green's function corresponding to one of the diffusion equations in (15), (16), or (17). Using this in (26), (27), together with $g(x,y)$ as data at $t=1$, great benefit derives from the ability to perform the deconvolution in *slow motion* by marching backward in time in the diffusion equation $w_t=-Lw$. Recall from section 2 that convolution of an $L^1(R^2)$ image $f(x,y)$ with a psf $h(x,y)$ leads to a blurred image $g(x,y)$ with $\|\ g\ \|_1=\|\ f\ \|_1$. However, as shown in (5), deconvolution of $g(x,y)$ with a psf $k(x,y)$ that is *"wider"* than $h(x,y)$ need not preserve L^1 norms. In such an image, legitimate high frequency components are falsely overamplified, leading to severe ringing and other artifacts, even in the absence of any noise in $g(x,y)$. This is oversharpening. Continuation all the way to $t=0$ in (26), (27), with $\hat{h}(\xi,\eta,t)$ as in (28), is equivalent to falsely setting $c=0$ in (8), thereby deblurring $g(x,y)$ with a psf that is *too wide*. This necessarily produces oversharpening. Displaying the evolution of the image $w^\dagger(x,y,t_n)$ in (27), as t_n decreases from 1 to 0, together with the accompanying diagnostic information $\|\ w^\dagger(.,t_n)\ \|_1$, $\|\ \nabla w^\dagger(.,t_n)\ \|_1$, allows for monitoring the deblurring process. At first, deconvolution is well behaved, with $\|\ w^\dagger(.,t_n)\ \|_1$ remaining constant, while $\|\ \nabla w^\dagger(.,t_n)\ \|_1$ increases monotonically, reflecting the gradual sharpening of edges and other localized singularities as $t_n\downarrow 0$. However, inevitably, ringing, noise, and other artifacts begin to appear in the image $w^\dagger(x,y,t_n)$, as high frequency components are falsely overamplified. A time $t_\#>0$ is reached such that both $\|\ w^\dagger(.,t_n)\ \|_1$ and $\|\ \nabla w^\dagger(.,t_n)\ \|_1$ increase monotonically for $0\le t_n<t_\#$.

5.1. Terminating continuation and selecting an optimal image. For $0\le t_n<t_\#$, the increase in $\|\ \nabla w^\dagger(.,t_n)\ \|_1$ primarily reflects increasing noise, while the increase in $\|\ w^\dagger(.,t_n)\ \|_1$ is due to oversharpening. It may seem natural to choose $w^\dagger(x,y,t_\#)$ as the optimal image. However, visual monitoring shows that image quality is usually already degraded at $t=t_\#$, and the best image is typically found at some $\overline{t}>t_\#>0$. Terminating continuation at $\overline{t}>0$ is equivalent to redefining $p(\rho)$ in (28) to be $\overline{p}(\rho)=(1-\overline{t})p(\rho)$, and then selecting the image at $t=0$ as optimal. Clearly, $\overline{t}$ corresponds to the unknown constant c in (8). The ability to adjust the otf and corresponding image interactively, in the manner described above, is an essential component of the present methodology.

In practice, the image L^1 norm may show a modest increase as t decreases from $t=1$ to $t=\overline{t}$. Conservation of the L^1 norm in $w^\dagger(x,y,t)$ can be enforced for any desired t by rescaling $w^\dagger(x,y,t)$ to the value $\|\ g\ \|_1$.

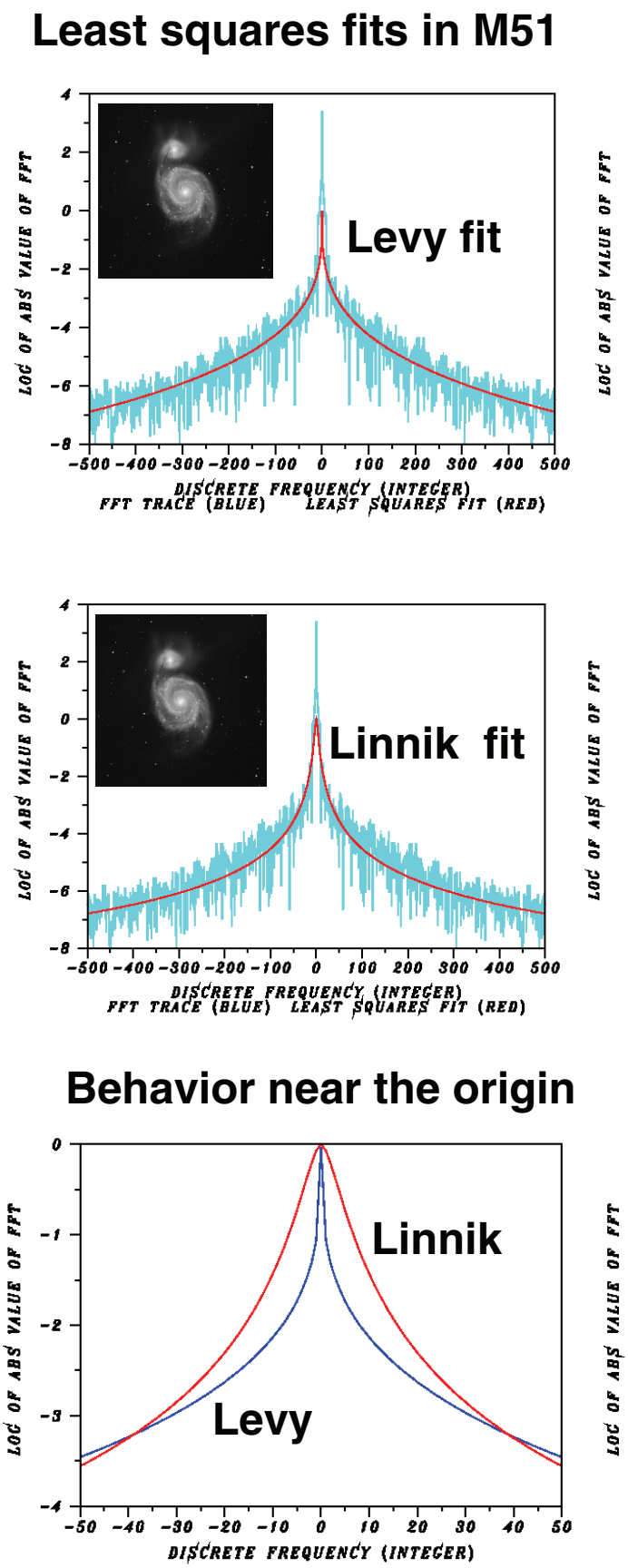

Figure 3. *Blurred M51 image data* $\log|\hat{g}(\xi,0)|$ *can be well fitted with a Lévy stable otf, as well as with a generalized Linnik otf. Both otfs have similar behavior away from the origin but differ fundamentally near the origin. This difference will play a crucial role.*

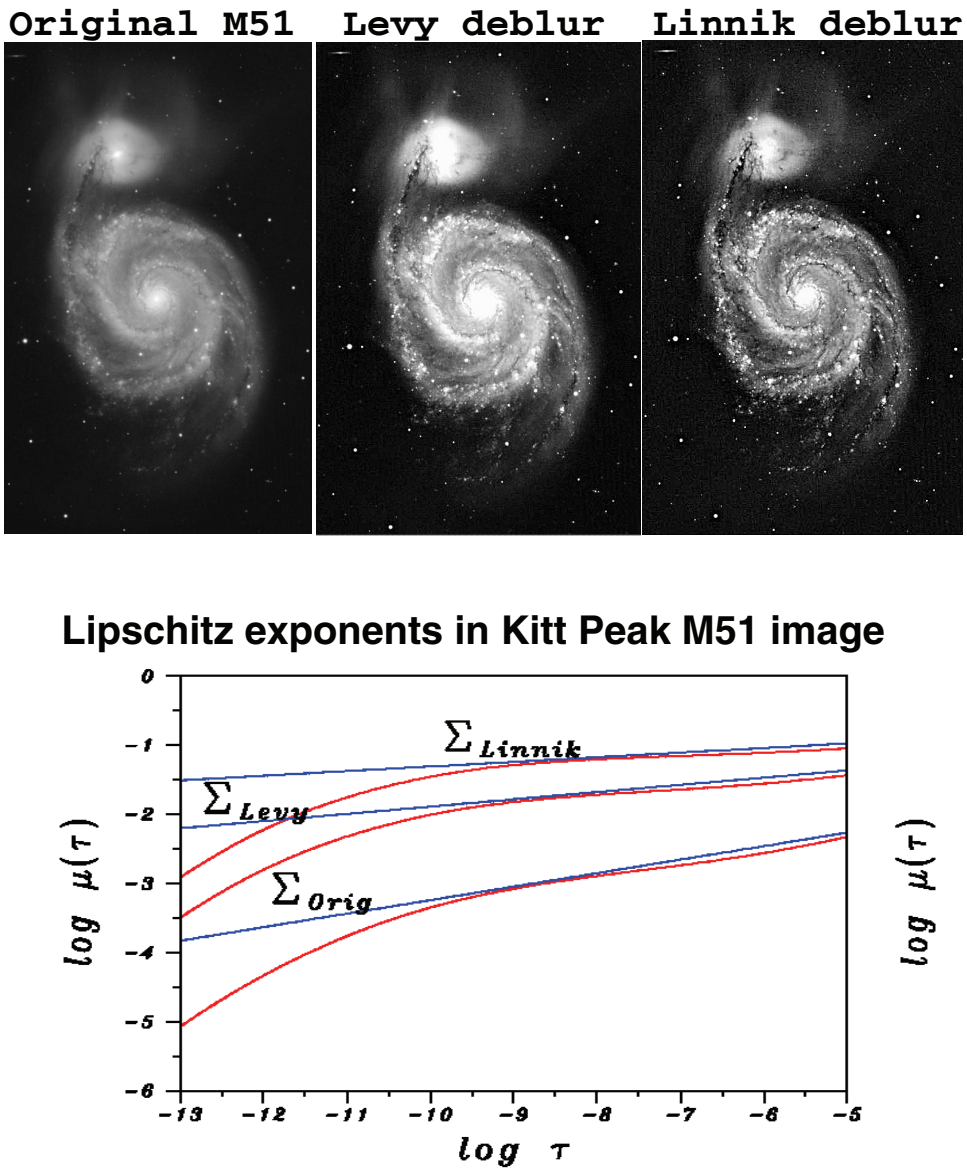

Figure 4. *The logarithmic diffusion equation produces higher quality reconstruction of the Whirlpool galaxy image than does the fractional diffusion equation. Such differences in quality are reflected in the smallness of the image Lipschitz exponent, which equals twice the slope of the corresponding* Σ *line. Here, the original image has Lip* $\alpha = 0.39$*, the Lévy image has Lip* $\alpha = 0.21$*, and the Linnik image has Lip* $\alpha = 0.13$*.*

6. Logarithmic vs. fractional diffusion in Whirlpool galaxy image. We shall now demonstrate the significance of the preceding developments by applying them to sharpen real blurred images with unknown blurs, subject to real but unknown noise processes. Our first example is a 1024×1024 pixel image $g(x, y)$ of the Whirlpool galaxy (M51), taken by Travis Rector and Monica Ramirez at the Kitt Peak National Observatory (NOAO/AURA/NSF) (National

Optical Astronomy Observatory/Associated Universities for Research in Astronomy/National Science Foundation).

In Figure 3, we examine the data $\log|\hat{g}(\xi,0)|$. With $\rho=\sqrt{\xi^2+\eta^2}$, we first consider a Lévy stable fit using $\hat{h}(\rho)=\exp(-\delta\rho^{2\beta}),\ \delta>0,\ 0<\beta\le 1$. While a Gaussian otf ($\beta=1.0$) is an allowed possibility, the monotone convexity property in $\log|\hat{g}(\xi,0)|$ forces $\beta\le 0.5$, which precludes Gaussians. The resulting least squares fit yields $\delta=1.07,\ \beta=0.15$. Next, with $w(x,y,1)=g(x,y)$, we solve the fractional diffusion equation $w_t=-\left[b(-\Delta)^{\beta}\right]w,\ 0\le t\le 1,\ b=\delta(4\pi^2)^{-\beta}$, backward in time, using an FFT implementation of (26), (27). With the regularization parameters $K=40.0,\ s=0.001$, the optimal image was found at $\overline{t}=0.75$. The L^1 norm was conserved on $\overline{t}\le t\le 1.0$, while the TV norm increased almost fourfold. The reconstructed image is the middle image at the top of Figure 4. The value $2\beta=0.30$ for the Lévy exponent is much lower than what is typically found in most physical applications of Lévy stable laws.

The analysis in section 3 emphasizes the behavior of $\hat{h}(\rho)$ away from the origin and makes it plausible that the system otf might be identifiable from that behavior. For blurred imagery with monotone convex Fourier decay, low exponent Lévy stable laws are natural candidate otfs in blind deconvolution. The fundamental observation of this paper is that there exist otfs with behavior away from the origin that is almost identical to that in low exponent Lévy stable laws, yet with behavior near the origin that is almost Gaussian. Indeed, consider a generalized Linnik fit to the same M51 data $\log|\hat{g}(\xi,0)|$, using $\hat{h}(\rho)=(1+\gamma\rho^{2\sigma})^{-\lambda},\ \gamma,\ \lambda>0,\ 0<\sigma\le 1$, as shown in Figure 3. This results in $\sigma=0.86,\ \gamma=0.09,\ \lambda=0.821$. The bottom drawing in Figure 3 illustrates the major difference between Levy and Linnik otfs near the origin. We next solve the logarithmic diffusion problem, $w_t=-\left[\lambda\log\{1+c(-\Delta)^{\sigma}\}\right]w,\quad c=\gamma(4\pi^2)^{-\sigma},\ 0\le t\le 1,\ w(x,y,1)=g(x,y)$, backward in time, using (26), (27). Here, with $K=40.0,\ s=0.001$ in (25), we now find the optimal image at $\overline{t}=0.65$. Again the L^1 norm was conserved on $\overline{t}\le t\le 1.0$, but the TV norm increased almost sevenfold. The reconstructed image is the rightmost image at the top of Figure 4.

Clearly, while the Lévy deblurred image significantly sharpens the original, the Linnik deblurred image provides higher quality reconstructions of the spiral arms, dustlanes, and galactic cores. The image Lipschitz exponent, discussed below, is a valuable image metrology tool that can measure the extent of fine structure recovery in deblurring and can quantify any improvement produced using logarithmic rather than fractional diffusion equations. This tool will be used throughout this paper.

7. Fine structure recovery and image Lipschitz exponents. An image $f(x,y)$ has L^1 Lipschitz exponent α if and only if

$$\int_{\mathbf{R^2}}|f(x+h_1,y+h_2)-f(x,y)|dxdy\le \textit{Constant}\ |h|^{\alpha},\qquad |h|\to 0, \tag{29}$$

where $|h|=(h_1^2+h_2^2)^{1/2}$, and α is fixed with $0<\alpha\le 1$. Most images are not smoothly differentiable functions of x and y but display edges, localized sharp features, and other significant fine scale details or *texture*. The Lipschitz exponent measures the fine structure content of an image, provided that image is relatively noise-free. The value of α decreases with increasing fine structure. An image that is of bounded variation, or smoother, has $\alpha=1$.

Most natural images have $\alpha < 0.6$ and are not of bounded variation. Images of starfields, galaxies, and clusters of galaxies often have $\alpha < 0.3$.

In [8], [13], an effective method for estimating image Lipschitz exponents is developed, based on a major theorem in [34]. For fixed $\tau > 0$, define the linear operator G^τ by means of the Fourier series

$$G^\tau f = \sum_{\xi,\eta=-\infty}^{\infty} \exp\{-\tau(\xi^2+\eta^2)\}\hat{f}(\xi,\eta)\exp\{2\pi i(x\xi+y\eta)\}. \tag{30}$$

Let $\mu(\tau) = \| G^\tau f - f \|_1 / \| f \|_1$ be the L^1 relative error in approximating f with $G^\tau f$. An image $f(x,y)$ has Lipschitz exponent α if and only if $\mu(\tau) = O(\tau^{\alpha/2})$ as $\tau \downarrow 0$. Using FFT algorithms, (30) can be evaluated for each fixed $\tau_n > 0$ in a sequence $\{\tau_n\}$ tending to zero, together with $\mu(\tau_n)$. By plotting $\mu(\tau_n)$ vs. τ_n on a log-log scale, positive constants C and α can be located such that $\mu(\tau) \le C\ \tau^{\alpha/2}$ as $\tau \downarrow 0$.

The three red curves in the bottom drawing in Figure 4 are plots of $\mu(\tau)$ vs. τ for each image in Figure 4. Each plot is majorized by a blue straight line Σ. The Lipschitz exponent α of each image is equal to twice the slope of the corresponding Σ line. Accordingly, the original M51 image has Lip $\alpha = 0.39$. The Lévy deblurred image has Lip $\alpha = 0.21$, indicating significant sharpening of the original. However, the Linnik deblurred image has Lip $\alpha = 0.13$, a striking improvement.

8. Tail behavior in physical space and resolution of mysterious Lévy exponents in [10], [11]. The improved reconstruction of M51 using the Linnik otf is directly traceable to the difference in behavior near the origin in the bottom drawing in Figure 3. As can be inferred from that drawing, selecting the Lévy otf rather than the Linnik otf implicitly declares the low frequencies in the blurred image $g(x,y)$ to be significantly more attenuated than would be implied by the Linnik otf. Consequently, in deblurring with the fractional diffusion equation, such low frequencies are necessarily amplified to a larger extent than would occur using the logarithmic diffusion equation. Such spurious overamplification causes saturation and loss of resolution in the galactic cores and spiral arms in the Lévy image. To mitigate this effect, the exit point $\overline{t}$ in the Lévy case must generally be chosen larger than in the Linnik case, which leads to less sharpening. As shown in Figure 5, such Lévy image saturation phenomena near the galactic cores are fairly common. As will be seen below, Linnik otf behavior near the origin plays a beneficial role in all the blind deconvolution experiments in this paper.

In physical (x,y) space, both the isotropic two-dimensional Lévy stable and generalized Linnik probability densities are *heavy-tailed densities*. However, although the corresponding characteristic functions can have the almost identical high frequency behavior shown in Figure 3, the tail behavior in physical (x,y) space in these two psfs can be distinctly different, as exemplified in Figure 2. Indeed, such tail behavior is directly related to the smoothness of the characteristic function near the origin in Fourier (ξ,η) space. The following important theoretical results may be found in [26]:

$$\begin{aligned} &\hat{h}_{Levy}(\xi,\eta) = \exp(-\delta\rho^{2\beta}), \quad \delta > 0, \quad 0 < \beta < 1, \quad \rho = \sqrt{(\xi^2+\eta^2)}, \\ &\Longrightarrow \quad h_{Levy}(x,y) = O\left(R^{-2-2\beta}\right), \quad R \uparrow \infty, \quad R = \sqrt{(x^2+y^2)}. \end{aligned} \tag{31}$$

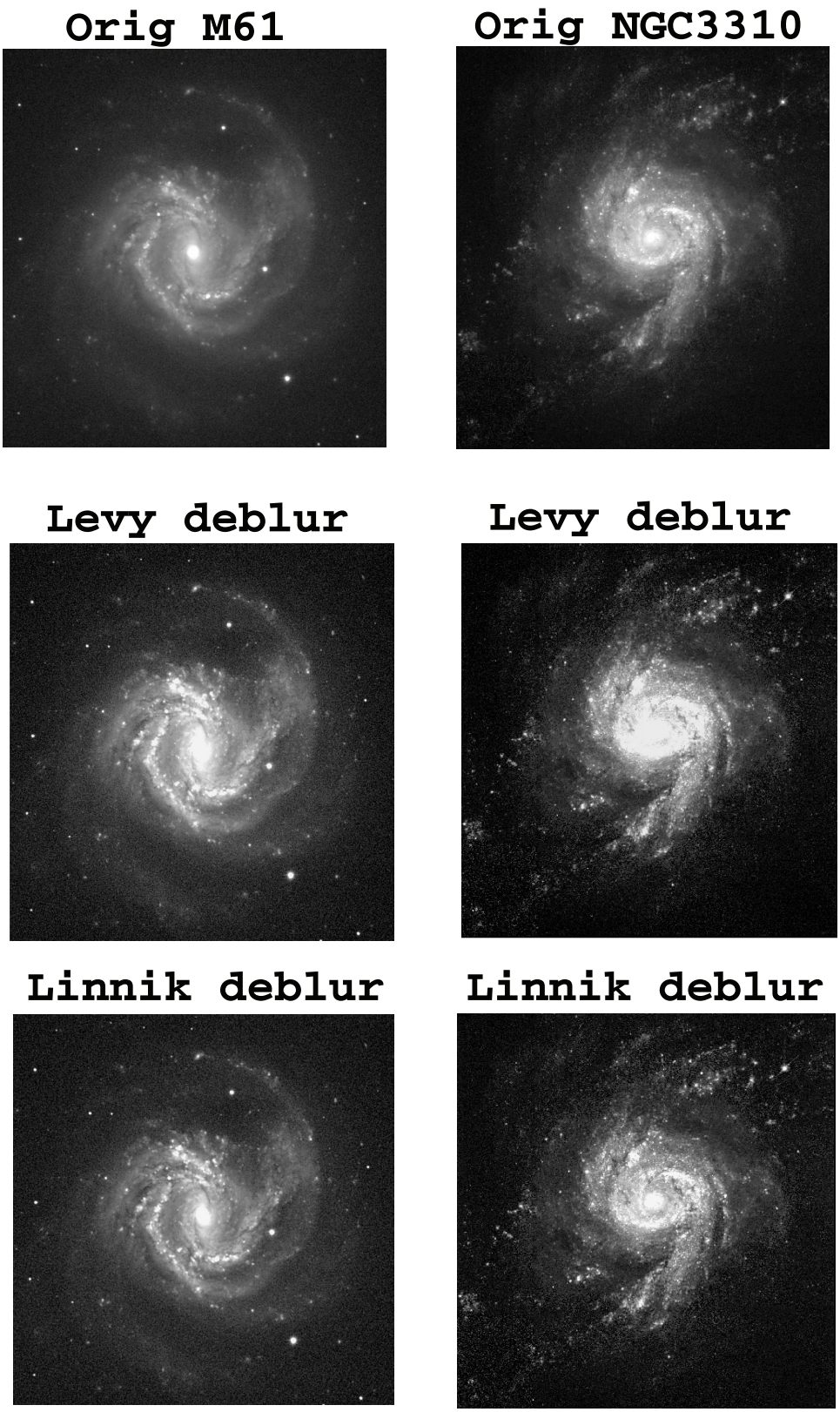

Figure 5. *Fractional diffusion processing generally causes saturation and loss of resolution near galactic cores, due to the behavior of Lévy stable otfs near the origin, as shown in Figure 3. The use of logarithmic diffusion avoids this difficulty.*

$$\begin{aligned} &\hat{h}_{Linn}(\xi,\eta) = (1+\gamma\rho^{2\sigma})^{-\lambda}, \quad \gamma,\ \lambda > 0, \quad 0 < \sigma < 1, \quad \rho = \sqrt{(\xi^2+\eta^2)}, \\ &\Longrightarrow \quad h_{Linn}(x,y) = O\left(R^{-2-2\sigma}\right), \quad R \uparrow \infty, \quad R = \sqrt{(x^2+y^2)}. \end{aligned} \tag{32}$$

Applied to the M51 image in Figure 3, where $\delta = 1.07$, $\beta = 0.15$, $\sigma = 0.86$, $\gamma = 0.09$, and $\lambda = 0.821$, this leads to

$$h_{Levy}(x,y) = O\left(R^{-2.3}\right), \qquad h_{Linn}(x,y) = O\left(R^{-3.72}\right), \quad R \uparrow \infty. \tag{33}$$

Thus, the Linnik density has a much thinner tail than the Lévy density in physical space. In summary, in the Whirlpool galaxy image in Figure 3, *the successful generalized Linnik psf has the tail behavior of a Lévy stable density with exponent* $2\beta = 1.72$ *in physical* (x,y) *space, but the high-frequency behavior of a stable density with* $2\beta = 0.30$ *in Fourier* (ξ,η) *space.* Similar behavior characterizes the successful Linnik otfs in other blind deconvolution experiments in this paper. This result resolves the unexplained appearance of exceptionally low Lévy exponents in the detected successful Lévy otfs in [10] and [11]. Clearly, such low exponents are not physically meaningful, but stem from choosing Lévy stable otfs, rather than generalized Linnik otfs, to match monotone convex high-frequency behavior in the blurred image data in [10] and [11].

9. Logarithmic diffusion and Hubble space telescope imagery. It is remarkable that the seemingly naive methodology developed in the previous sections can be useful in improving Hubble imagery. However, in many cases, faint background objects can be made more visible, and the structure of foreground objects can become more clearly defined. This appears to be possible for the third-generation instrument known as the Advanced Camera for Surveys (ACS), recently repaired in May 2009, as well as for the "workhorse" Wide Field and Planetary Camera 2 (WFPC2), replaced with WFPC3 in May 2009. The on-line version of this paper will be helpful in the subsequent discussion. Credit for the three images to be deconvolved below includes NASA (National Aeronautics and Space Administration), ESA (European Space Agency), the Hubble Heritage Team (STScI/AURA) (Space Telescope Science Institute/Association of Universities for Research in Astronomy), A. Riess (STScI), and K. Noll (STScI).

1. *Pinwheel galaxy NGC* 1309. The example at the top of Figure 6 is a February 2006 Hubble telescope image of the spiral galaxy NGC 1309. The image was taken with Hubble's most powerful camera, the Advanced Camera for Surveys. NASA describes this image as featuring bright bluish clusters of star formation, together with dust lanes spiraling into a yellowish central core of older-population stars. The image is complemented by far-off background galaxies. This galaxy is also home to a supernova that can help astronomers measure the expansion rate of the universe.

Considerable enhancement of these features is possible using logarithmic diffusion. The color image was broken up into its constituent red, green, and blue component images (RGB), and each component was treated in turn. For each component, $\log|\hat{g}(\xi,0)|$ was best fitted with the generalized Linnik otf expression $\hat{h}(\rho) = (1+\gamma\rho^{2\sigma})^{-\lambda}$, $\gamma,\ \lambda > 0$, $0 < \sigma \leq 1$. For the blue component, this results in $\gamma = 0.174$, $\lambda = 0.653$, and $\sigma = 0.88$. Otfs for the other two components were found to differ only slightly from the blue component otf. The

Figure 6. *Successful blind deconvolution of Hubble space telescope NGC* 1309 *image. The original blue component image has Lip* $\alpha = 0.25$. *The Linnik blue component has Lip* $\alpha = 0.09$.

Figure 7. *Successful blind deconvolution of Hubble space telescope NGC* 6050 *image. The original blue component image has Lip* $\alpha = 0.28$. *The Linnik blue component has Lip* $\alpha = 0.15$.

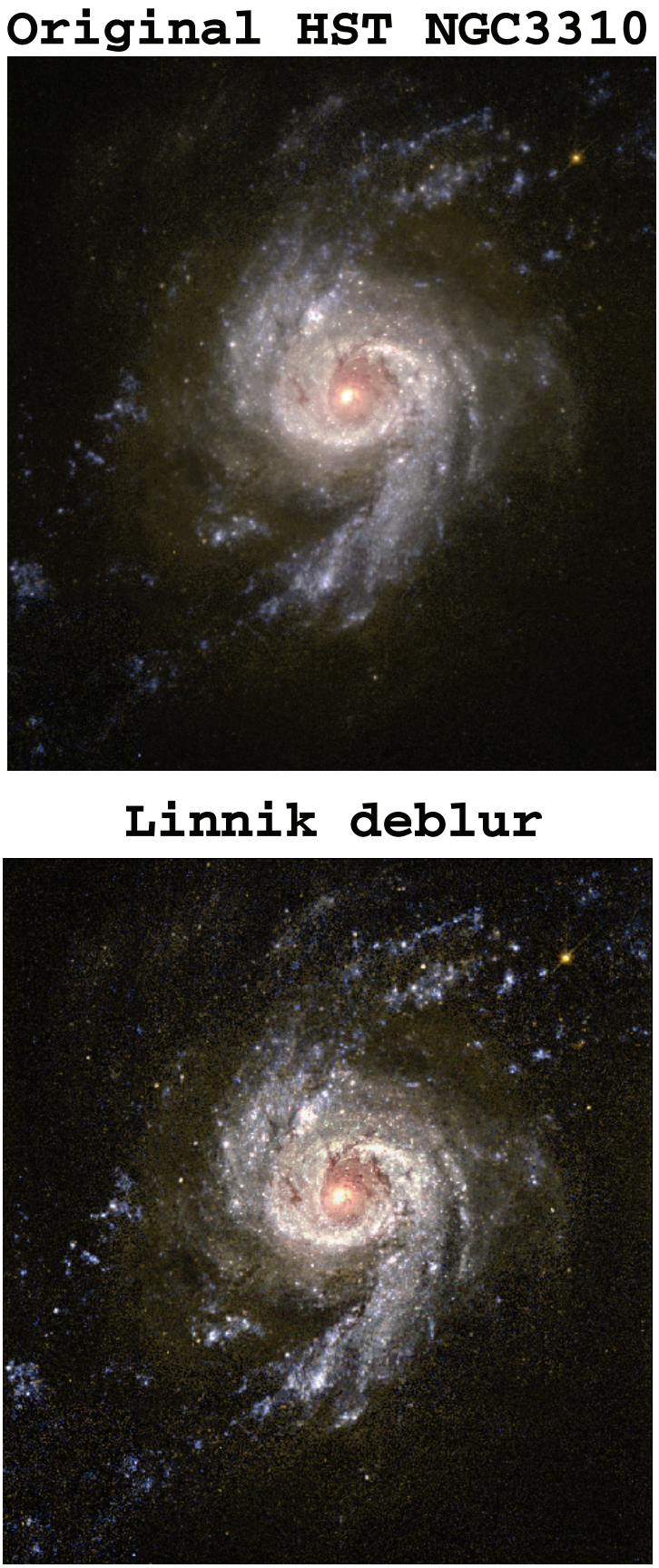

Figure 8. *Successful blind deconvolution of Hubble space telescope NGC* 3310 *image. The original red component image has Lip* $\alpha = 0.26$. *The Linnik red component has Lip* $\alpha = 0.14$.

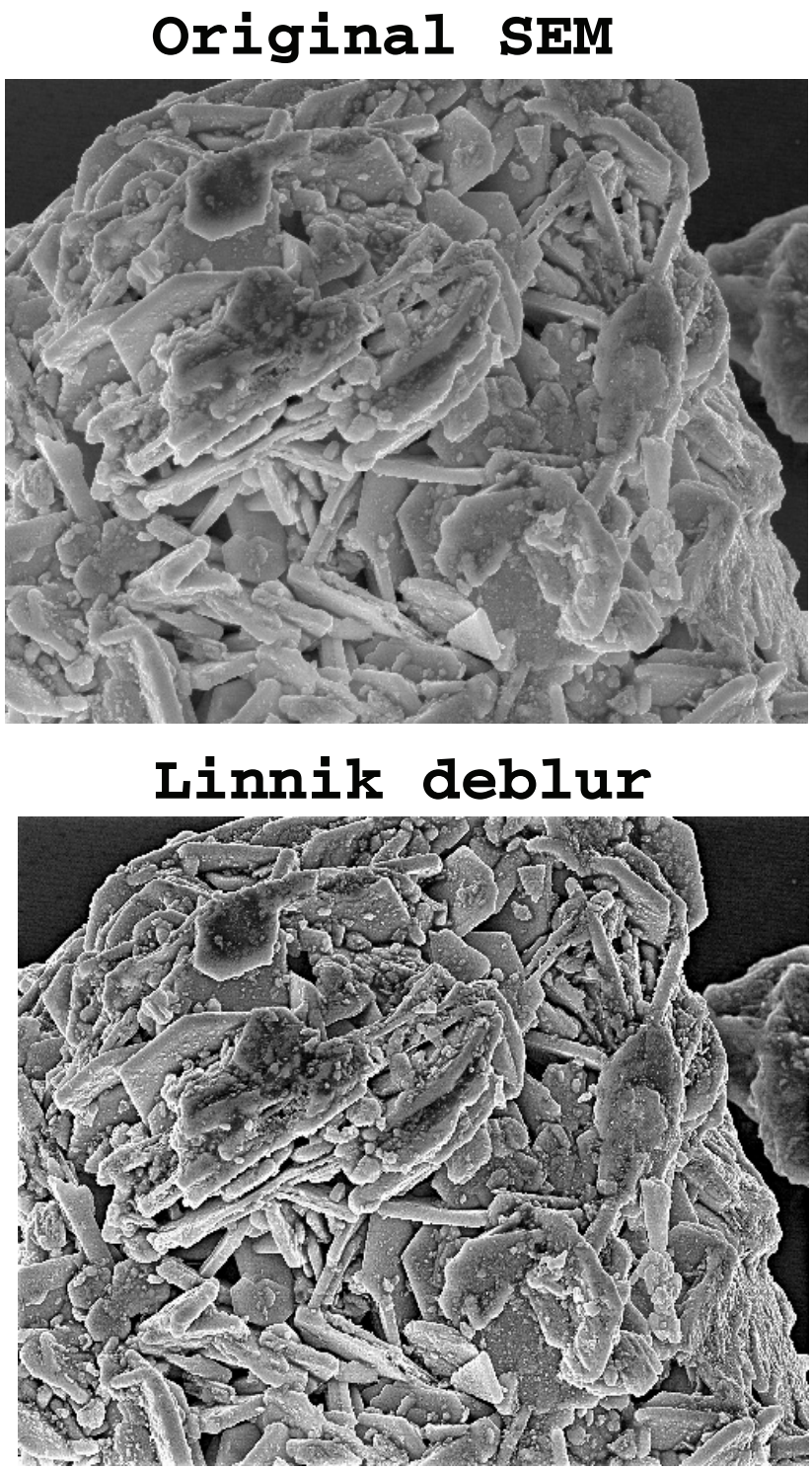

Figure 9. *Blind deconvolution of scanning electron micrograph of complex crystalline structure recovers numerous surface particles and other fine detail. The original image has Lip* $\alpha = 0.37$. *The Linnik image has Lip* $\alpha = 0.20$.

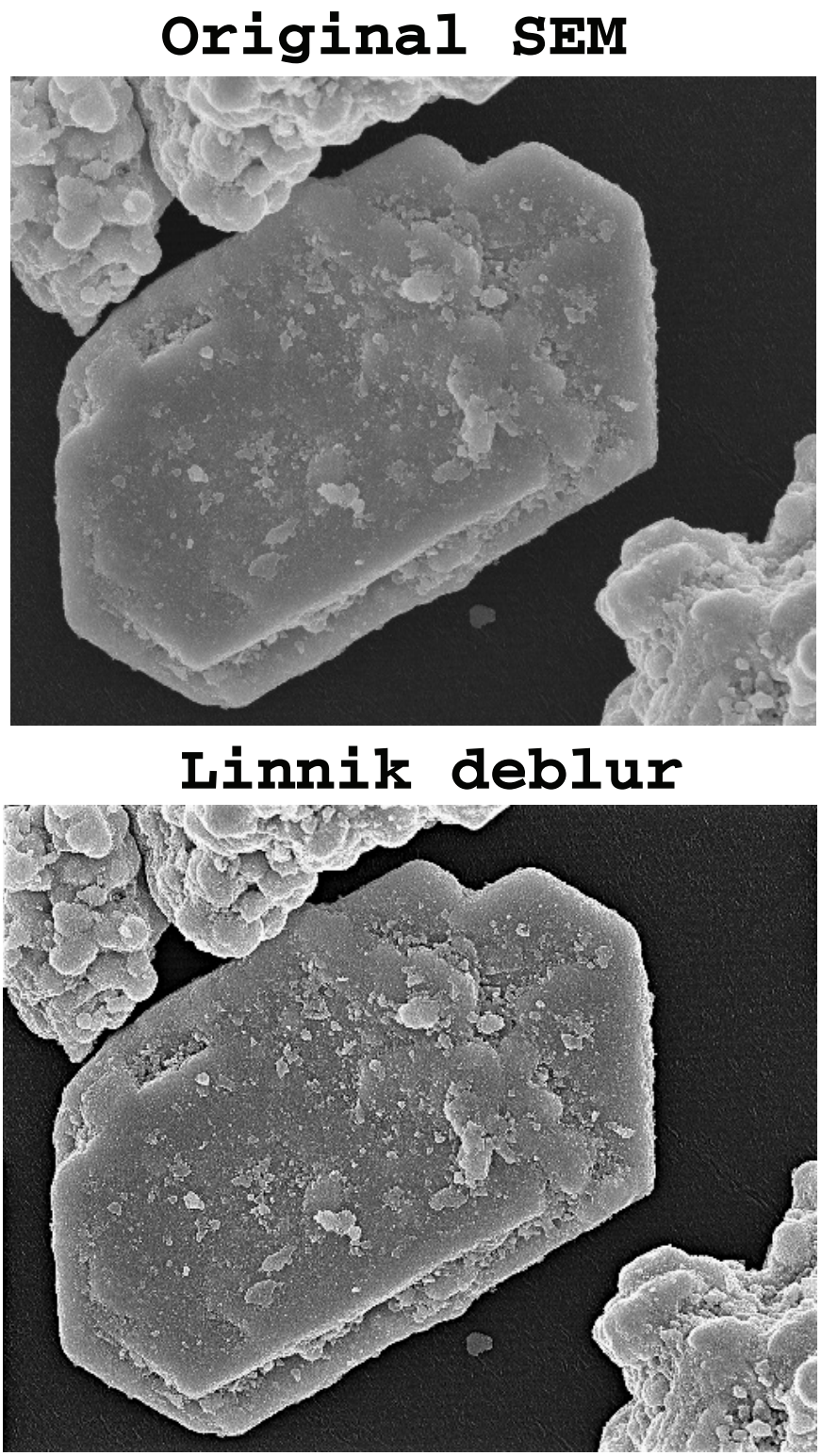

Figure 10. *Blind deconvolution of scanning electron micrograph of slab like crystalline structure recovers fine scale detail. Note the improvement in the corner structures. The original image has Lip* $\alpha = 0.48$. *The Linnik image has Lip* $\alpha = 0.25$.

latter was therefore used for all three components. We next solve the logarithmic diffusion problem, $w_t = -[\lambda \log\{1 + c(-\Delta)^\sigma\}]\, w, \quad c = \gamma(4\pi^2)^{-\sigma},\ 0 \le t \le 1, \quad w(x, y, 1) = g(x, y)$, backward in time, using (26), (27). In all three cases, with the regularization parameters $K = 40.0,\ s = 0.001$ and with $\overline{t} = 0.7$, the L^1 norm was conserved on $1 \ge t \ge \overline{t}$, without rescaling, while the TV norm increased fivefold.

The Linnik deblurred image is shown at the bottom of Figure 6. At the outskirts of that image, several far-off galaxies have become more visible, and the scythe-shaped structure at eleven o'clock is now brighter and more clearly defined. Previously barely visible outer spiral arms have been recovered, along with a multitude of previously faint stars. Within the galaxy's main body, the bluish star clusters along the spiral arms, and the dust lanes are now much better resolved.

Evidently, significant fine-structure reconstruction was achieved, and this is reflected in Lipschitz exponents. For the blue component, the original image has Lip $\alpha = 0.25$, while the Linnik image has Lip $\alpha = 0.09$. Lévy deblurring of the blue component required termination at $\overline{t} = 0.8$ and displayed loss of resolution due to saturation. That image had Lip $\alpha = 0.12$.

2. *Colliding galaxies NGC* 6050. The example at the top of Figure 7 involves a spectacular collision between two spiral galaxies. That image is part of a large collection of similar images released by NASA in April 2008. Acquired using Hubble's Wide Field and Planetary Camera 2, the image represents a rarely observed snapshot of a galactic merger thought to require several hundred million years to complete. It is believed that the Milky Way and Andromeda galaxies will eventually merge in a similar fashion.

In applying logarithmic diffusion to this image, distinct generalized Linnik otfs $\hat{h}(\rho) = (1 + \gamma\rho^{2\sigma})^{-\lambda},\ \gamma, \lambda > 0,\ 0 < \sigma \le 1$, were obtained for each RGB component. The $(\gamma,\ \lambda,\ \sigma)$ triplet for each component was as follows: red = (0.195, 0.692, 0.85); green = (0.201, 0.643, 0.88); and blue = (0.151, 0.684, 0.83). We next solve the logarithmic diffusion problem, $w_t = -[\lambda \log\{1 + c(-\Delta)^\sigma\}]\, w,\ c = \gamma(4\pi^2)^{-\sigma},\ 0 \le t \le 1,\ w(x, y, 1) = g(x, y)$, backward in time, using (26), (27). In all three cases, with $K = 100,\ s = 0.001$, and $\overline{t} = 0.75$, the L^1 norm was conserved on $1 \ge t \ge \overline{t}$, without rescaling, while the TV norm increased by a factor of about 3.5.

The Linnik image at the bottom of Figure 7 is noticeably brighter and displays better resolution of the structural details in the two galaxies. Bluish young star clusters along spiral arms are better defined, together with dust lanes spiraling around the three cores of older stars. Background galaxies have become more visible. As a result, significant reduction in Lipschitz exponents was recorded. For the blue component, the original image has Lip $\alpha = 0.28$, while the Linnik image has Lip $\alpha = 0.15$. Lévy deblurring of the blue image resulted in Lip $\alpha = 0.18$.

3. *Starburst galaxy NGC* 3310. The example at the top of Figure 8 is a September 2001 Hubble telescope image of the Starburst galaxy NGC 3310, acquired using the Wide Field and Planetary Camera 2. That galaxy is of great interest to astronomers as it is known to produce clusters of new stars at a prodigious rate. Several hundred such clusters are visible as bright blue diffuse objects around the galaxy's spiral arms, each cluster representing up to a million stars.

In applying logarithmic diffusion to this image, the Linnik otf parameters for the red component were found to be $\gamma = 0.328,\ \lambda = 0.557$, and $\sigma = 0.92$. The red and blue otfs almost coincided, while the green otf differed slightly. Accordingly, the red image otf

was used for all three components. We next solve the logarithmic diffusion problem, $w_t = -[\lambda \log\{1 + c(-\Delta)^\sigma\}]\, w$, $c = \gamma(4\pi^2)^{-\sigma}$, $0 \le t \le 1$, $w(x, y, 1) = g(x, y)$, backward in time, using (26), (27). In all three cases, with $K = 40.0$, $s = 0.001$, and $\overline{t} = 0.75$, the L^1 norm increased by about 3% on $1 \ge t \ge \overline{t}$, with a threefold increase in the TV norm. Rescaling was applied to conserve L^1 norms prior to displaying the deblurred image.

The Linnik deblurred image at the bottom of Figure 8 shows significant recovery of blue clusters of young stars at the periphery of the image; also, there is noticeable enhancement of structural detail in the main body of the galaxy and in the surrounding dust lanes. In contrast, Lévy deblurring tends to produce saturation and loss of resolution near the core, as previously shown in Figure 4. For the red component, the original image has Lip $\alpha = 0.26$, while the Linnik image has Lip $\alpha = 0.14$. The Lévy image has Lip $\alpha = 0.16$.

10. Scanning electron micrographs. There are other important classes of images which display the monotone convex behavior described in section 2, and for which logarithmic diffusion deconvolution may be useful. One such class is scanning electron micrographs. In this section, we revisit experiments previously described in [11], and we verify that Linnik otfs can improve substantially on previous results. The two images considered here were taken by John Small at NIST. They are micrographs of a complex multiform crystalline compound of mercury. The author expresses his gratitude to Dr. David S. Bright (NIST) for making these images available.

The example at the top of Figure 9 has complex crystalline structure and fine scale surface detail that are of interest. The Linnik otf parameters for $\log|\hat{g}(\xi, 0)|$ were found to be $\gamma = 0.0266$, $\lambda = 0.5496$, and $\sigma = 0.89$. We next solve the logarithmic diffusion problem, $w_t = -[\lambda \log\{1 + c(-\Delta)^\sigma\}]\, w$, $c = \gamma(4\pi^2)^{-\sigma}$, $0 \le t \le 1$, $w(x, y, 1) = g(x, y)$, backward in time, using (26), (27). With $K = 50.0$, $s = 0.001$, and $\overline{t} = 0.6$, the L^1 norm was conserved on $1 \ge t \ge \overline{t}$ without rescaling, and there was a threefold increase in the TV norm. The Linnik image at the bottom of Figure 9 shows recovery of numerous surface particles and other details, and the complex morphology has become better defined. Deblurred image quality is particularly noticeable in this example. The original image has Lip $\alpha = 0.37$, and the Linnik image has Lip $\alpha = 0.20$. The Lévy image was terminated at $\overline{t} = 0.7$ and had Lip $\alpha = 0.25$.

The slab-like structure at the top of Figure 10 also exhibits interesting surface detail. The Linnik otf parameters were found to be $\gamma = 0.022$, $\lambda = 0.776$, and $\sigma = 0.86$. With $K = 50.0$, $s = 0.001$, and $\overline{t} = 0.7$, the L^1 norm was conserved on $1 \ge t \ge \overline{t}$ without rescaling, and there was a threefold increase in TV norm. Here again, slab surface details are well recovered, and the two corner structures reveal interesting small scale granularity. The original image has Lip $\alpha = 0.48$, and the Linnik image has $\alpha = 0.25$. The Lévy image was terminated at $\overline{t} = 0.75$ and had Lip $\alpha = 0.34$.

Table 1 below summarizes the changes in image Lipschitz exponents recorded in each of the six deconvolution experiments in this paper. This is a valuable metric that can quantify the degree of fine structure recovery, provided the reconstructed image is relatively noise-free. Linnik deblurring consistently produces smaller Lipschitz exponents than does Lévy deblurring. The last column in Table 1 is especially noteworthy.

11. Concluding remarks. A priori knowledge about the solution is an essential element in the successful computation of ill-posed inverse problems. Such knowledge informs the con-

Table 1
Lipschitz exponents before and after deconvolution.

Image	Original lip	Lévy lip	Linnik lip	Linnik/Orig
M 51	$\alpha = 0.39$	$\alpha = 0.21$	$\alpha = 0.13$	33 %
NGC 1309	$\alpha = 0.25$	$\alpha = 0.12$	$\alpha = 0.09$	36 %
NGC 6050	$\alpha = 0.28$	$\alpha = 0.18$	$\alpha = 0.15$	53 %
NGC 3310	$\alpha = 0.26$	$\alpha = 0.16$	$\alpha = 0.14$	54 %
SEM Crystal	$\alpha = 0.37$	$\alpha = 0.25$	$\alpha = 0.20$	54 %
SEM Slab	$\alpha = 0.48$	$\alpha = 0.34$	$\alpha = 0.25$	52 %

struction of the blind deconvolution procedure discussed in this paper. This methodology was shown to be capable of producing credible reconstructions in two distinct classes of real blurred images with real noise, one at the nanoscale, and the other at the cosmological scale. These two classes are acquired using distinct imaging modalities and are of considerable scientific interest. The accompanying sizeable reduction in Lipschitz exponents is highly significant.

This work substantially improves on previous work on the same classes of images [10], [11] based on isotropic Lévy stable otfs. In that early work, low Lévy exponents were found to be necessary to accommodate the monotone convex high frequency Fourier behavior in the blurred image data. As shown in section 4, Lévy stable motions are related to Brownian motion through subordination. The present work is based on a new class of otfs that have the same high frequency behavior as low exponent stable otfs but behave like high exponent stable laws near the origin. Such generalized Linnik otfs result from subordination of Lévy stable motions by the Gamma process, and their behavior near the origin was shown to play a vital role in fine structure recovery. The compelling quality of the new reconstructions strongly suggests that the detected generalized Linnik otfs that produce these results must emulate essential aspects of the true system otfs in the two classes of images. Linnik otfs are not currently known in image analysis.

Sixty years after its introduction in [5], Bochner's seminal mathematical idea continues to yield a rich harvest of important applications.

REFERENCES

[1] C. Albanese and S. Lawi, *Time quantization and q-deformations*, J. Phys. A, 37 (2004), pp. 2983–2987.

[2] L. Bar, N. Sochen, and N. Kiryati, *Semi-blind image restoration via Mumford-Shah regularization*, IEEE Trans. Image Process., 15 (2006), pp. 483–493.

[3] P. Barthelemy, J. Bertolotti, and D. S. Wiersma, *A Lévy flight for light*, Nature, 453 (2008), pp. 495–498.

[4] S. Bochner, *Monotone Funktionen, Stieltjes Integrale und harmonische Analyse*, Math. Ann., 108 (1933), pp. 378–410.

[5] S. Bochner, *Diffusion equation and stochastic processes*, Proc. Nat. Acad. Sci. U.S.A., 35 (1949), pp. 368–370.

[6] S. Bochner, *Harmonic Analysis and the Theory of Probability*, University of California Press, Berkeley, CA, 1955.

[7] A. S. Carasso, *The APEX method in image sharpening and the use of low exponent Lévy stable laws*, SIAM J. Appl. Math., 63 (2002), pp. 593–618.

[8] A. S. Carasso, *Singular integrals, image smoothness, and the recovery of texture in image deblurring*, SIAM J. Appl. Math., 64 (2004), pp. 1749–1774.

[9] A. S. Carasso, *False characteristic functions and other pathologies in variational blind deconvolution. A method of recovery*, SIAM J. Appl. Math., 70 (2009), pp. 1097–1119.
[10] A. S. Carasso, *APEX blind deconvolution of color Hubble space telescope imagery and other astronomical data*, Optical Engineering, 45 (2006), 107004.
[11] A. S. Carasso, D. S. Bright, and A. E. Vladár, *APEX method and real-time blind deconvolution of scanning electron microscope imagery*, Optical Engineering, 41 (2002), pp. 2499–2514.
[12] A. S. Carasso and T. Kato, *On subordinated holomorphic semigroups*, Trans. Amer. Math. Soc., 327 (1991), pp. 867–878.
[13] A. S. Carasso and A. E. Vladár, *Calibrating image roughness by estimating Lipschitz exponents, with applications to image restoration*, Optical Engineering, 47 (2008), 037012.
[14] T. F. Chan and C. K. Wong, *Total variation blind deconvolution*, IEEE Trans. Image Process., 7 (1998), pp. 370–375.
[15] I. Eliazar and J. Klafter, *Lévy, Ornstein-Uhlenbeck, and subordination: Spectral vs. jump description*, J. Statist. Phys., 119 (2005), pp. 165–196.
[16] M. B. Erdogan and I. V. Ostrovskii, *Analytic and asymptotic properties of generalized Linnik probability densities*, J. Math. Anal. Appl., 217 (1998), pp. 555–578.
[17] G. Fasshauer, *Meshfree Approximation Methods with MATLAB*, Interdiscip. Math. Sci. 6, World Scientific, Singapore, 2007.
[18] W. Feller, *An Introduction to Probability Theory and Its Applications, Vol.* 2, 2nd ed., Wiley, New York, 1971.
[19] V. Ganti, A. Singh, P. Passalacqua, and E. Foufoula-Georgiou, *Subordinated Brownian motion model for sediment transport*, Phys. Rev. E, 80 (2009), 011111.
[20] H. Geman, D. P. Madan, and M. Yor, *Time changes for Lévy processes*, Math. Finance, 11 (2001), pp. 79–96.
[21] C. B. Johnson, *Classification of electron-optical device modulation transfer function*, Advances in Electronics and Electron Physics, 33B (1972), pp. 579–584.
[22] C. B. Johnson, *MTFs: A simplified approach*, Electro-Optical Systems Design, 4 (1972), pp. 22–26.
[23] C. B. Johnson, *Point-spread functions, line-spread functions, and edge-response functions associated with mtfs of the form* $exp[-(\omega/\omega_c)^n]$, Appl. Optics, 12 (1973), pp. 1031–1033.
[24] L. Justen and R. Ramlau, *A non-iterative regularization approach to blind deconvolution*, Inverse Problems, 22 (2006), pp. 771–800.
[25] J. Lee and D. Sheen, *F. John's stability conditions versus A. Carasso's SECB constraint for backward parabolic problems*, Inverse Problems, 25 (2009), 055001.
[26] S. C. Lim and L. P. Teo, *Analytic and asymptotic properties of multivariate generalized Linnik's probability densities*, J. Fourier Anal. Appl., 16 (2010), pp. 715–747.
[27] E. Lukacs, *Characteristic Functions*, 2nd ed., Griffin, London, 1970.
[28] D. P. Madan and E. Seneta, *The Variance Gamma model for share market returns*, J. Business, 63 (1990), pp. 511–524.
[29] D. P. Madan, P. P. Carr, and E. C. Chang, *The Variance Gamma process and option pricing*, European Finance Rev., 2 (1998), pp. 79–105.
[30] R. S. Phillips, *On the generation of semigroups of linear operators*, Pacific J. Math., 2 (1952), pp. 343–369.
[31] G. Samorodnitsky and M. S. Taqqu, *Stable Non-Gaussian Random Processes: Stochastic Models with Infinite Variance*, Chapman and Hall, New York, 1994.
[32] K. Sato, *Lévy Processes and Infinitely Divisible Distributions*, Cambridge University Press, Cambridge, UK, 1999.
[33] I. J. Schoenberg, *Metric spaces and completely monotone functions*, Ann. of Math., 39 (1938), pp. 811–841.
[34] M. H. Taibleson, *On the theory of Lipschitz spaces of distributions on Euclidean n-space.* I. *Principal properties*, J. Math. Mech., 13 (1964), pp. 407–479.
[35] A. Weron and M. Magdziarz, *Anomalous diffusion and semimartingales*, Europhys. Lett., 86 (2009), 60010.